How to cite: *Angew. Chem. Int. Ed.* **2025**, *64*, e202500771
doi.org/10.1002/anie.202500771

Polymer Chemistry **Hot Paper**

Aqueous Self-Assembly of Cylindrical and Tapered Bottlebrush Block Copolymers

Clark Vu[+], Narjess Abu Amara[+], Mohammed Alaboalirat, Einat Nativ-Roth, Ran Zalk, Wellington Leite, Jan-Michael Carrillo, Ronit Bitton, and John B. Matson**

Abstract: The self-assembly of amphiphilic bottlebrush block copolymers (BCPs), featuring backbones densely grafted with two types of side chains, is less well understood compared to linear BCPs. In particular, the solution self-assembly of tapered bottlebrush BCPs—cone-shaped BCPs with hydrophilic or hydrophobic tips—remains unexplored. This study investigates eight tapered and four cylindrical bottlebrush BCPs with varied ratios of hydrophobic polystyrene (PS) and hydrophilic poly(acrylic acid) (PAA) side chains, synthesized via sequential addition of macromonomers using ring-opening metathesis polymerization (SAM-ROMP). Self-assembled nanostructures formed in water were analyzed using cryogenic transmission electron microscopy, small-angle neutron scattering, and dynamic light scattering. Most BCPs generated multiple nanostructures with surface protrusions, including spherical micelles, cylindrical micelles, and vesicles, alongside transitional forms like ellipsoids and semi-vesicles. Coarse-grained molecular dynamics simulations supported the experimental findings, which revealed two distinct self-assembly pathways. The first involved micelle fusion, producing elliptical and cylindrical aggregates, sometimes forming Y-junctions. The second pathway featured micelle maturation into semivesicles, which developed into vesicles or large compound vesicles. This work provides the first experimental evidence of vesicle formation via semivesicles in bottlebrush BCPs and demonstrates the significant influence of cone directionality on self-assembly behavior in these cone-shaped polymeric amphiphiles.

Introduction

Aqueous self-assembly of amphiphilic block copolymers (BCPs) has been the subject of intense research for several decades due to their wide-ranging applications, including as catalytic microreactors, templates for the formation of inorganic nanoparticles, drug delivery vehicles, viscosity modifiers, and many others.[1–3] Traditional self-assembled morphologies of linear amphiphilic BCPs include spheres, cylinders, and vesicles, and in many cases, the dominant morphology can be predicted based on guidelines defined by Israelachvili for small molecule surfactants[4] and adapted by Eisenberg for linear BCPs based on interfacial curvature.[5] These different morphologies influence the functions of these nanostructures; for example, worm-like BCP nanostructures have extended circulation half-lives versus spherical structures,[6] and various BCP nanostructures can template the formation of hard nanoparticles with control over size and shape.[7] Decades of research have focused mainly on solution self-assembly of centrosymmetric linear BCPs, with some effort devoted to self-assembly of more topologically complex but still largely symmetric BCPs including star polymers, cyclic polymers, dendrimers, dendronized polymers, and bottlebrush polymers.[8,9]

Of these more complex polymer topologies, self-assembly studies on bottlebrush BCPs have recently gained significant

[*] C. Vu[+], J. B. Matson
Department of Chemistry, Virginia Tech, Blacksburg, VA 24061, USA
E-mail: jbmatson@vt.edu

C. Vu[+], M. Alaboalirat, J. B. Matson
Macromolecules Innovation Institute, Virginia Tech, Blacksburg, VA 24061, USA

N. Abu Amara[+], R. Bitton
Department of Chemical Engineering, Ben-Gurion University of the Negev, Beer-Sheva, Israel
E-mail: rbitton@bgu.ac.il

E. Nativ-Roth, R. Zalk, R. Bitton
Ilse Katz Institute for Nanoscale Science and Technology, Ben-Gurion University of the Negev, Beer-Sheva, Israel

W. Leite
Neutron Scattering Division, Oak Ridge National Laboratory, Oak Ridge, TN 37831, USA

J.-M. Carrillo
Center for Nanophase Materials Sciences, Oak Ridge National Laboratory, Oak Ridge, TN 37831, USA

[+] Both authors contributed equally to this work.

Additional supporting information can be found online in the Supporting Information section

interest.[10–16] Comprised of a polymer backbone with densely grafted polymeric side chains, bottlebrush polymers can assume worm-like or rod-like conformations in solution. The dense packing of the side chains causes extension of the backbone polymer and also drastically limits entanglements or other interactions between individual bottlebrush macromolecule chains.[17–19] When two different types of side chains are attached to a single backbone, e.g., hydrophilic side chains on one end and hydrophobic side chains on the other, amphiphilic bottlebrush BCPs can self-assemble with features that differ from amphiphilic linear BCPs. For example, the critical micelle concentrations in bottlebrush BCPs are typically lower and less sensitive to polymer molecular weight than in linear BCPs.[20–22] They also tend to self-assemble with lower aggregation number (N_{agg}) values than linear polymers. More complex bottlebrush polymer structures, such as ABC triblock or ABCD tetrablock copolymers, also lead to interesting self-assembled morphologies such as onion-like layered nanostructures.[23,24] A substantial body of computational studies, relying primarily on coarse-grained molecular dynamics simulations, have helped to explain and predict the evolution of bottlebrush BCP morphologies in solution.[25–28] Linear–bottlebrush BCPs, where only one component is a bottlebrush polymer, are just beginning to be explored (primarily in the solid phase thus far), and a large study showed shifts in the phase boundaries for traditional solid-state morphologies as well as significant phase coexistence.[29]

These examples highlight the rich self-assembled nanostructures accessible to bottlebrush BCPs and their derivatives, but most examples focus on BCPs with a high degree of symmetry. A few research groups have introduced side chains of variable lengths to self-assembled bottlebrush BCPs; for example, Rzayev,[30,31] Alexander-Katz,[32] and Kim[33] have all studied the solution self-assembly behavior of amphiphilic bottlebrush BCPs with tunable side chain lengths. In all cases, they have found that side chain length impacts self-assembled morphology. However, amphiphilic bottlebrush BCPs with a tunable cone-shape have never been explored.

Experimental studies on the self-assembly of cone-shaped units have thus far focused primarily on Gemini surfactants,[34] small dendrimers,[35–37] amphiphiles containing polyhedral oligomeric silsesquioxane (POSS) units,[38–40] and micron-sized colloids.[41,42] The solid-state self-assembled morphologies of these disparate types of cone-shaped amphiphiles have revealed assembly modes not often observed with symmetrical building blocks such as quasicrystal phases; solution self-assembly studies of cone-shaped dendrimers have also uncovered 2-dimensional aggregates such as toroids and other unusual morphologies.[43] These experimental results are supported by computational work in this area,[44–47] including a finding by Glotzer and coworkers that cone-shaped amphiphiles can self-assemble into more highly ordered and more monodisperse aggregates than their symmetric (cylindrical) analogs.[44] These examples suggest a potentially rich self-assembly landscape in cone-shaped (tapered) bottlebrush BCPs.

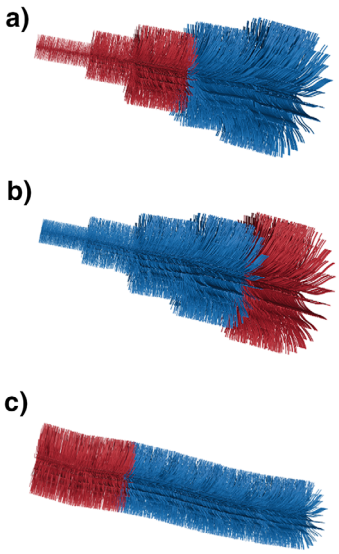

Figure 1. Schematic illustrations of tapered bottlebrush BCPs containing hydrophilic side chains (blue) and hydrophobic side chains (red). a) A tapered bottlebrush BCP with a hydrophobic tip. b) A tapered bottlebrush BCP with a hydrophilic tip. c) A cylindrical bottlebrush BCP.

Tapered bottlebrush polymers take on a cone-shaped, 3D structure because they contain side chain polymers with systematically varied molecular weights. Recent advances have enabled the synthesis of tapered bottlebrush homopolymers and BCPs (Figure 1a–b),[48–51] but their self-assembly has never been evaluated. We began exploring the synthesis and self-assembly of this unusual polymer class because they provide the ability to control not only hydrophilic/hydrophobic ratio, a critical factor in self-assembly of all types of BCPs, but also cone directionality, i.e., the position of the two types of blocks along the cone, either a hydrophilic tip or a hydrophobic tip. We envisioned that a systematic study of cone-shaped bottlebrush BCP amphiphiles, in comparison with cylindrical bottlebrush BCPs (Figure 1c), could begin to reveal the self-assembly landscape of these large, non-centrosymmetric amphiphiles.

Here, we set out to synthesize a systematic series of tapered bottlebrush BCPs, along with structurally analogous cylindrical bottlebrush BCPs. Leveraging a synthetic method developed in our lab termed sequential addition of macromonomers ring-opening metathesis polymerization (SAM-ROMP),[48] which allows for precise control of the size, shape, and placement of hydrophobic and hydrophilic side chains, we aimed to study how these unique polymer amphiphiles self-assemble in solution. We hypothesized that structural parameters influencing cone shape and directionality would influence the type and distribution of self-assembled morphologies of these polymer amphiphiles. Using several characterization techniques, we describe here our initial exploration into the self-assembly of this unusual class of polymer amphiphiles.

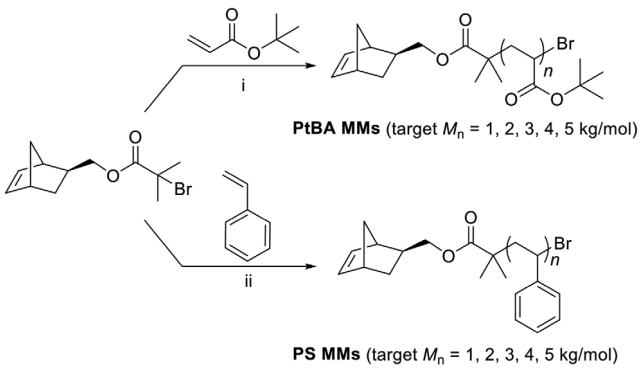

Scheme 1. Synthesis of PtBA and PS MMs.[a] [a] Conditions: (i) Cu(I)Br, Cu(II)Br, PMDETA, acetone, 60 °C, 5 h. (ii) Cu(I)Br, Cu(II)Br, PMDETA, DMF, 90 °C, 8 h. Target molecular weights (1, 2, 3, 4, and 5 kg mol^{-1}) for each correspond approximately to target N_{sc} (n) values of 10, 20, 30, 40, and 50.

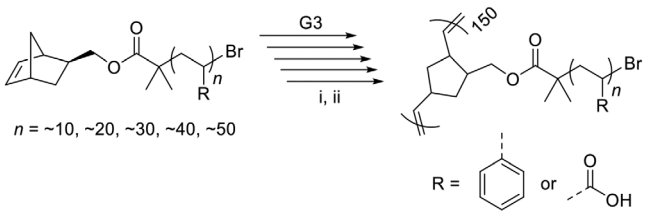

Scheme 2. SAM-ROMP synthesis of amphiphilic tapered bottlebrush BCPs with PS and PAA side chains.[a]
[a] Conditions: i) 1. EtOAc, rt; 2. Ethyl vinyl ether. ii) HCl, HFIP, rt, 4 h.

Results and Discussion

Design and Synthesis of Amphiphilic Tapered Bottlebrush BCPs

We set out to synthesize a library of tapered bottlebrush BCPs using the SAM-ROMP method.[48] In brief, SAM-ROMP involves two steps: 1) Synthesis of a series of monotelechelic macromonomers (MMs) of varying degrees of polymerization (i.e., molar mass) with a norbornene unit on one end; 2) Sequential "grafting-through" ROMP of several macromonomers (we typically use five) with either increasing or decreasing molar mass. This process generates a cone-shaped bottlebrush polymer. Guironnet has developed elegant continuous addition approaches to make tapered bottlebrush polymers,[50,51] but we utilized the SAM-ROMP approach here because it enables purification and full characterization of each MM before the SAM-ROMP process is carried out.

In this work, we prepared two sets of MMs, one based on polystyrene (PS) and one based on poly(*tert*-butyl acrylate) (PtBA), each with target side chain molar masses of 1, 2, 3, 4, and 5 kg mol^{-1} (Scheme 1, Table S1, and Figures S3–S14). The PS MMs, termed S^{1K}, S^{2K}, S^{3K}, S^{4K}, and S^{5K}, with "S" representing PS and the superscript designating the approximate molar mass, served as the hydrophobic components. We chose PtBA for the other set of MMs, T^{1K}, T^{2K}, T^{3K}, T^{4K}, and T^{5K}, with T representing PtBA, because the *tert*-butyl esters could be hydrolyzed to form hydrophilic poly(acrylic acid) (PAA) side chains, enabling the construction of tapered bottlebrush BCPs with varying amounts of hydrophilic and hydrophobic content. All 10 MMs were synthesized using atom-transfer radical polymerization (ATRP) following a recently described approach.[52] A critical component was the choice of anchor group, which describes the atoms linking the polymer side chain to the polymerizable norbornene unit.[53,54] Fast MM conversion is critical in the SAM-ROMP synthesis of tapered bottlebrush BCPs because extended reaction periods result in catalyst activity loss and, as a result, poor control over the final tapered bottlebrush BCP structure.

After ATRP synthesis reached the target molar mass, each MM was extensively purified because contaminants including residual vinyl monomer, ligand, Cu species, or their decomposition products can affect the propagation rate and ultimate degree of polymerization in ROMP, both of which are critical for a living polymerization. We purified the PS MMs using automated gradient chromatography, similar to Lawrence and coworkers,[55] to remove unreacted monomer, residual Cu and ligand, and coupled MM products. In a similar manner, we purified and isolated each of the PtBA MMs. Finally, to test each batch of MM, we performed one-shot ROMP reactions on each using Grubbs third generation catalyst (**G3**, $(H_2IMes)(Cl)_2(pyr)_2RuCHPh$) as the ROMP initiator at a [MM]/[**G3**] ratio of 100. We then characterized the bottlebrush polymer products by size exclusion chromatography with multi-angle light scattering (SEC-MALS) to verify that each test polymerization reached the expected molar mass and exhibited a monomodal and narrowly dispersed peak (Figures S15 and S16).

With this set of 10 MMs in hand, we performed SAM-ROMP to make eight different tapered bottlebrush BCPs, each with five MM blocks with sequential side-chain molar masses of 1, 2, 3, 4, and 5 kg mol^{-1} (Scheme 2). These molar mass values align approximately with side-chain degrees of polymerization (N_{sc}) values of 10, 20, 30, 40, and 50. All SAM-ROMP reactions were performed at rt in EtOAc due to its ability to provide fast propagation rates.[56] Preparatory ROMP kinetics experiments targeting backbone degrees of polymerization (N_{bb}) of 30 for each block were carried out for 5 kg mol^{-1} PS and PtBA macromonomers to determine the best timing before injecting the next MM. Allowing too little or too much time is detrimental to the topology of the bottlebrush BCPs due to incomplete conversion of the MMs and premature catalyst death, respectively. Kinetics experiments revealed a half-life of approximately 0.5 min for both 5 kg mol^{-1} MMs, and we determined that polymerizing for approximately five half-lives (2.5 min) was sufficient for clean chain extension.

SAM-ROMP reactions were performed from bigger to smaller molecular weight MMs. We targeted a total N_{bb} for each tapered bottlebrush BCP of 150 (i.e., an N_{bb} of 30 for each block) in order to ensure that we exceeded the globule-to-brush transition that Verduzco established to occur above DP ~120 in a set of bottlebrush copolymers with PS side chains.[57] Removal of an aliquot of the reaction mixture before each MM addition allowed us to follow molar mass evolution over time using SEC-MALS. Values generally were

within 10%–20% of expected values, and the traces were all monomodal with small shoulders if any, and dispersity ($Đ$) values were generally < 1.1 (Figures S17–S20). Together, these results demonstrated the successful synthesis of eight tapered bottlebrush BCPs with polynorbornene backbones and a mixture of PS and P*t*BA side chains.

We also synthesized four cylindrical bottlebrush BCPs. These bottlebrush BCPs were prepared using sequential ROMP of just two different MMs, S^{3K} and T^{3K}, varying the block ratio to cover most of the hydrophobic weight percent range of the tapered BB BCPs. Molecular weight details and SEC traces are shown in Table S4 and Figure S21, respectively. These four polymers served as controls that did not assume a conical shape.

Following isolation and characterization of the 12 bottlebrush BCPs (8 tapered, 4 cylindrical), we needed to hydrolyze the *tert*-butyl ester groups to form amphiphilic tapered bottlebrush BCPs with PS and PAA side chains. Removal of *tert*-butyl esters is often executed by using an excess of trifluoroacetic acid (TFA) in CH_2Cl_2, but we opted instead to follow a recently published alternative procedure using HCl in hexafluoroisopropanol (HFIP) because it demonstrated faster kinetics than the TFA and CH_2Cl_2 procedure with quantitative removal of the *tert*-butyl group based on ^{1}H NMR spectroscopy (Scheme 2, Figures S22–S33).[58] This procedure was done for all bottlebrush BCPs, affording the desired series of 12 amphiphilic tapered bottlebrush BCPs (Table 1).

Critical to this work, our SAM-ROMP approach allowed us to make tapered bottlebrush BCPs with either hydrophobic tips (Figure 1a) or hydrophilic tips (Figure 1b). We envisioned that the cone-shaped nature of these bottlebrush BCPs would create asymmetry in the structures such that polymers with similar hydrophilic/hydrophobic ratios would assemble into different nanostructures or different distributions of nanostructures due to the different locations within the cone of the hydrophobic PS side chains (i.e., at the tip or the base). This cone/tip designation is a key feature of tapered bottlebrush BCPs that cannot be recapitulated in cylindrical bottlebrush BCPs (Figure 1c).

The polymers were named as follows: Each block is represented as $X_n{}^{yK}$ where X = type of side chain (S = PS, A = PAA, T = PtBA), yK = side chain molecular weight (in kg mol^{-1}), and n = backbone degree of polymerization for each block. Here, $n = 30$ for all blocks. For example, the amphiphilic tapered bottlebrush BCP with one hydrophobic tip block and four hydrophilic base blocks would be represented as: $S_{30}{}^{1K}A_{30}{}^{2K}A_{30}{}^{3K}A_{30}{}^{4K}A_{30}{}^{5K}$. Table 1 shows all 12 bottlebrush BCPs and includes the hydrophobic weight fraction, determined through SEC-MALS analysis of aliquots of the reaction mixture at each stage in the bottlebrush polymer synthesis (Tables S5 and S6).

Bottlebrush BCP Self-Assembly

Self-assembled nanostructures of the eight amphiphilic tapered bottlebrush BCPs and the four cylindrical bottlebrush BCPs were prepared using the solvent exchange method from THF into phosphate buffer solution (pH 7.4), similar to a previous publication (Figure S34).[20] Buffer was viewed as a critical component in order to avoid pH changes that could lead to changes in PAA protonation state among different samples. We chose phosphate buffer due to its biological relevance and our intent to evaluate these materials as drug delivery vehicles. Our method involved slow evaporation of THF, which should allow the aggregates to reach an equilibrium morphology or near-equilibrium distribution of morphologies.[59] The final sample concentration was 1 mg mL^{-1}. The samples were stored as solutions and characterized directly without additional modifications or treatments.

Table 1: Structural descriptions for each of the eight tapered bottlebrush BCPs (entries 1–8) and the four cylindrical bottlebrush BCPs (entries 9–12).

Entry	Structure[a]	wt% hydrophobic[b]	Estimated *p* value[c]
1	$S_{30}^{1K}A_{30}^{2K}A_{30}^{3K}A_{30}^{4K}A_{30}^{5K}$	9%	0.53
2	$S_{30}^{1K}S_{30}^{2K}A_{30}^{3K}A_{30}^{4K}A_{30}^{5K}$	20%	0.66
3	$S_{30}^{1K}S_{30}^{2K}S_{30}^{3K}A_{30}^{4K}A_{30}^{5K}$	54%	0.40
4	$S_{30}^{1K}S_{30}^{2K}S_{30}^{3K}S_{30}^{4K}A_{30}^{5K}$	65%	0.43
5	$A_{30}^{1K}S_{30}^{2K}S_{30}^{3K}S_{30}^{4K}S_{30}^{5K}$	96%	3.89
6	$A_{30}^{1K}A_{30}^{2K}S_{30}^{3K}S_{30}^{4K}S_{30}^{5K}$	83%	2.16
7	$A_{30}^{1K}A_{30}^{2K}A_{30}^{3K}S_{30}^{4K}S_{30}^{5K}$	71%	2.10
8	$A_{30}^{1K}A_{30}^{2K}A_{30}^{3K}A_{30}^{4K}S_{30}^{5K}$	53%	1.18
9	$S_{22}^{3K}A_{128}^{3K}$	21%	0.98
10	$S_{48}^{3K}A_{102}^{3K}$	42%	0.98
11	$S_{93}^{3K}A_{57}^{3K}$	69%	0.98
12	$S_{121}^{3K}A_{29}^{3K}$	90%	0.98

[a] Naming convention is based on the formula for each block of $X_n{}^{yK}$ where X = type of side chain (S = PS, A = PAA), yK = target side chain molecular weight (in kg mol^{-1}), and n = target backbone degree of polymerization (N_{bb}) for each individual block. Target side chain molecular weight and backbone N_{bb} values are noted; actual values based on SEC-MALS analysis are shown in Tables S5 and S6. [b] Hydrophobic wt% values were determined based on the molecular weights of the synthesized MMs and bottlebrush polymers as determined using SEC-MALS (Tables S2–S4); the polynorbornene backbone, which constitutes only a small percentage of the mass of each polymer, was not considered in these calculations. [c] Estimated *p* value refers to the Israelachvili packing parameter (described in Supporting Information section Estimation of Packing Parameters).

Application of Traditional Guidelines for Rationalizing Self-Assembled Nanostructures

We considered the amphiphilic BCP structures in the context of the Israelachvili packing parameter (p), a common method to explain and predict equilibrium morphologies in surfactants and amphiphilic polymers.[4,30,60,61] Packing parameters have also been previously used for analysis of symmetric and non-centrosymmetric bottlebrush BCP self-assembly.[30] In brief, p values can be calculated by estimating the hydrophobic volume (v), critical hydrophobic length (l_c), and hydrophilic head group area (a_0) for an individual amphiphile

according to the equation $p = v/(l_c a_o)$. In traditional surfactants, $p < 0.33$ predicts spherical structures, $0.33 < p < 0.5$ predicts cylindrical morphologies, $0.5 < p < 1$ predicts bilayer vesicles, and $p > 1$ predicts inverted structures.

In a previous study on asymmetric bottlebrush BCPs (i.e., those with different N_{sc} values for the two types of side chains, polylactide, PLA, and poly(ethylene glycol), PEG), Rzayev and coworkers applied an Israelachvili packing parameter analysis.[30] The authors found that asymmetric bottlebrush BCPs, prepared by direct dissolution of the polymer amphiphiles, self-assembled into nanostructures that mostly lined up with packing parameter predictions. They also rationalized the observed structures in terms of interfacial curvature, ultimately determining that a larger hydrophilic PEG N_{sc} compared to the hydrophobic PLA N_{sc} resulted in a higher curvature and, therefore, a lower packing parameter.

Assuming an extended structure due to the generally stiff nature of bottlebrush polymer backbones, we calculated p values for each of the 12 BCPs. In brief, values for l_c were calculated using a value for a fully extended polynorbornene repeating unit applied to a scaling law derived from our previous paper on cylindrical and tapered bottlebrush homopolymers.[49] Values for a_0 were calculated using a similar analysis based on a fully extended PAA repeating unit for the block with a PAA side chain at the hydrophobic–hydrophilic interface. Finally, values for v were calculated for each individual block using calculated length and area values, then summing the 1–4 cylindrical hydrophobic units to arrive at a volume of the hydrophobic portion for each bottlebrush BCP (described in Supporting Information section Estimation of Packing Parameters).

We found that p values for the hydrophobic tip tapered BCPs (BCPs **1**–**4**) hovered near 0.5, indicating that cylindrical morphologies should be preferred. In the case of hydrophilic-tip bottlebrush BCPs **5**–**8**, all p values were > 1, suggesting that inverted structures should form. Finally, p values for cylindrical BCPs **9**–**12** all were 0.98, suggesting that all four bottlebrush BCPs in this set should form vesicles.

Some guidelines for BCP self-assembly suggest that the Israelachvili packing parameter is not useful in many cases for rationalizing or predicting self-assembled morphologies for several reasons, including that the effective head group area depends on the molecular volume of the hydrophilic block and solvent quality.[62] Another problem is that in surfactant micelles, the hydrophilic head group is small and contributes little to the total volume of the assembly, but hydrophilic blocks in linear BCPs can be large, even larger than the hydrophobic blocks in many cases. Instead, wt% is often a better predictor for linear BCPs of self-assembled morphology in water, where BCPs with <~45 wt% hydrophobic content tend to assemble into spheres, those with ~45%–55 wt% tend to assemble into cylinders, and BCPs with ~60%–75 wt% hydrophobic content assemble largely into vesicles to minimize contact of the hydrophobic components with water.[63]

Based on these guidelines, we expected that tapered bottlebrush BCPs **1**–**2** would pack to form spheres because both had < 45 wt% hydrophobic content. Tapered bottlebrush BCPs **3** (54 wt% hydrophobic) and **4** (65 wt% hydrophobic) would then be expected to form cylinders and vesicles, respectively. For the hydrophilic tip series (BCPs **5**–**8**), all had > 45 wt% hydrophobic content, suggesting cylinders and vesicles. Finally, for the cylindrical BCP series (BCPs **9**–**12**), BCPs **9** and **10** (21 wt% and 42 wt% hydrophobic, respectively) should form spherical micelles, while BCPs **11** and **12** (69 and 90 wt% hydrophobic content, respectively) should form vesicles and potentially other lamellar structures.

Cryo-TEM Results

We analyzed the solution structure of the self-assembled aggregates using cryo-TEM. Images were collected at several magnification levels, and nearly all nanostructures showed extended protrusions on their surfaces, which we attribute to the polynorbornene backbone of the hydrophilic component (the PAA side chain units are highly hydrated and, therefore, invisible by cryo-TEM). Interestingly, the self-assembled BCPs rarely formed just one type of morphology. Therefore, we analyzed up to 700 nanostructures from several images of each to generate a plot of the nanostructure distributions for each self-assembled bottlebrush BCP (Figure 2).

*Hydrophobic Tip Tapered BCPs **1**–**4***

Selected images of the "hydrophobic tip" tapered bottlebrush BCPs (BCPs **1**–**4**) at varying levels of magnification are shown in Figure 3. BCP **1** (Figure 3a) self-assembled to form 100% spherical aggregates. Based on an analysis of their diameters, 90% of aggregates were spherical micelles, with 10% larger spheres, i.e., spheres with core diameters beyond the maximally extended hydrophobic tip. These larger spheres may be aggregates of individual bottlebrush BCPs with hydrophobic blocks larger than the average (due to molar mass dispersity in the BCPs) or semivesicles, which are structures transitioning from spherical micelles to vesicles that have not yet developed solvent-filled core.[64] Images of BCP **2** (Figure 3b) showed 99% spherical aggregates that were all spherical micelles (55%) and larger spheres (45%), which all resembled a micellar morphology. We also observed 1% ellipsoids (aspect ratio > 1.3). BCP **3** (Figure 3c) showed a rich variety of nanostructures where spherical micelles remained the dominant nanostructure but coexisted alongside ellipsoids and vesicles with a few large spherical structures and cylindrical micelles (aspect ratio > 3). BCP **4** (Figure 3d) also exhibited a range of nanostructures with cylindrical micelles as the dominant structure followed by spherical micelles and then ellipsoids. A small number of semivesicles and vesicles were also observed, along with some large compound vesicles, sometimes called multigenus vesicles,[65] and pearl necklace structures (counted here simply as vesicles and spherical micelles, respectively).

Qualitatively, the spherical micelles observed in assemblies of BCPs **1**–**4** followed the trend of linear BCPs, where an increase in hydrophobic block length moving from BCPs **1** to **2** to **3** to **4** resulted in a transition from "star-like" or "hairy" micelles with protrusions longer than the core to "crew-cut"

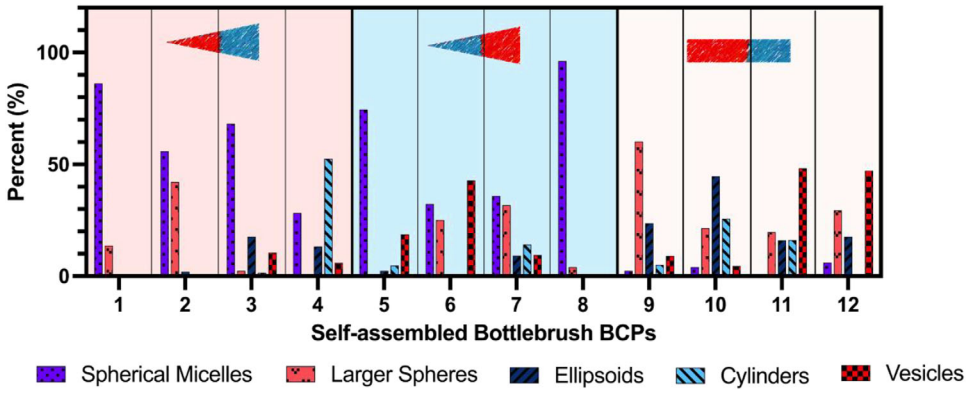

Figure 2. Distribution of morphologies in cryo-TEM images of self-assembled BCPs **1**–**12**. Morphology distributions were determined across the five categories shown by counting up to 700 individual particles for each bottlebrush BCP.

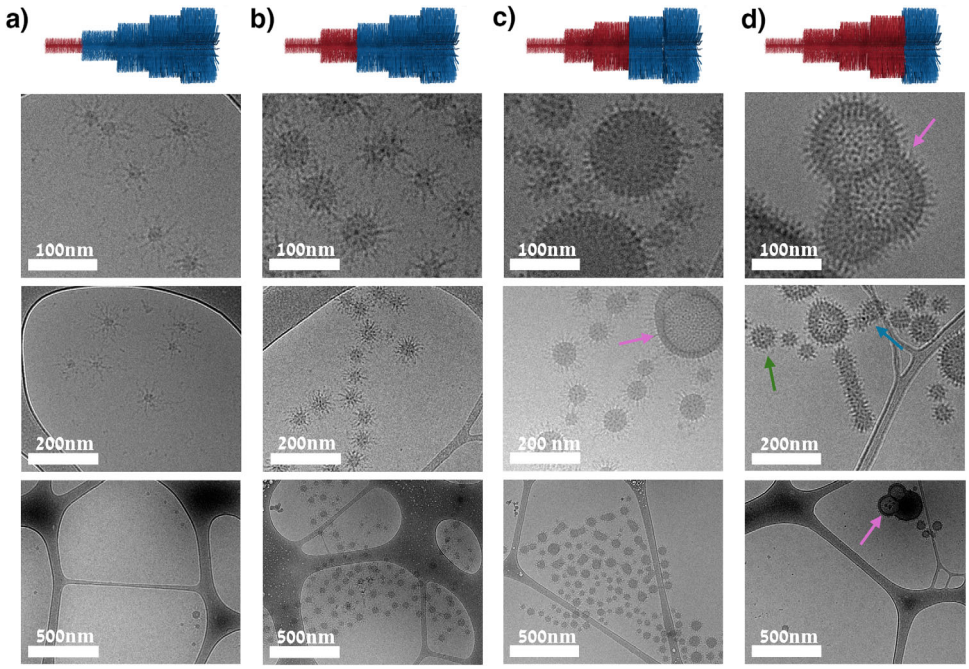

Figure 3. Cryo-TEM images of self-assembled aggregates of tapered bottlebrush BCPs **1**–**4** at three different levels of magnification. BCPs **1** and **2** (columns A and B, respectively) showed almost exclusively spherical nanostructures. BCP **3** (column C) showed a mixture of spheres, ellipsoids, and a few vesicles but no cylindrical structures. BCP **4** (column D) showed spheres, ellipsoids (blue arrow) cylinders, and vesicles, including several large compound vesicles (purple arrow) and semi-vesicles (green arrow). The middle image in this column highlights spherical micelles, a cylindrical aggregate, and vesicles all in the same frame.

micelles with protrusions shorter than the core diameter. We attribute the thin features that appear to be inside the core of the nanostructures to the polynorbornene backbones of hydrophilic components on the surface of the micelles or vesicles in these 2D images of 3D objects. These images also demonstrated that increasing hydrophobic content led to an increased variety of nanostructures and a smaller fraction of spherical micelles.

The variety of nanostructures coupled with the images of transitional structures suggests that these morphologies are either i) kinetically trapped or ii) lie along an energy landscape with several types of nanostructures of similar thermodynamic stability, as suggested by Eisenberg in studies on linear BCP solution self-assembly.[5] Heating tapered bottlebrush BCP solutions **2** and **4** to 80 °C followed by slow cooling to room temperature and subsequent cryo-TEM imaging showed similar types and distributions of nanostructures (Figure S36). These results suggest that explanation ii, i.e., the nanostructures have similar thermodynamic stability, is the more likely explanation for these self-assembled BCPs.

*Hydrophilic Tip Tapered BCPs **5**–**8***

Selected images of the self-assembled aggregates from BCPs **5**–**8** are shown in Figure 4. BCP **5** (Figure 4a), which was

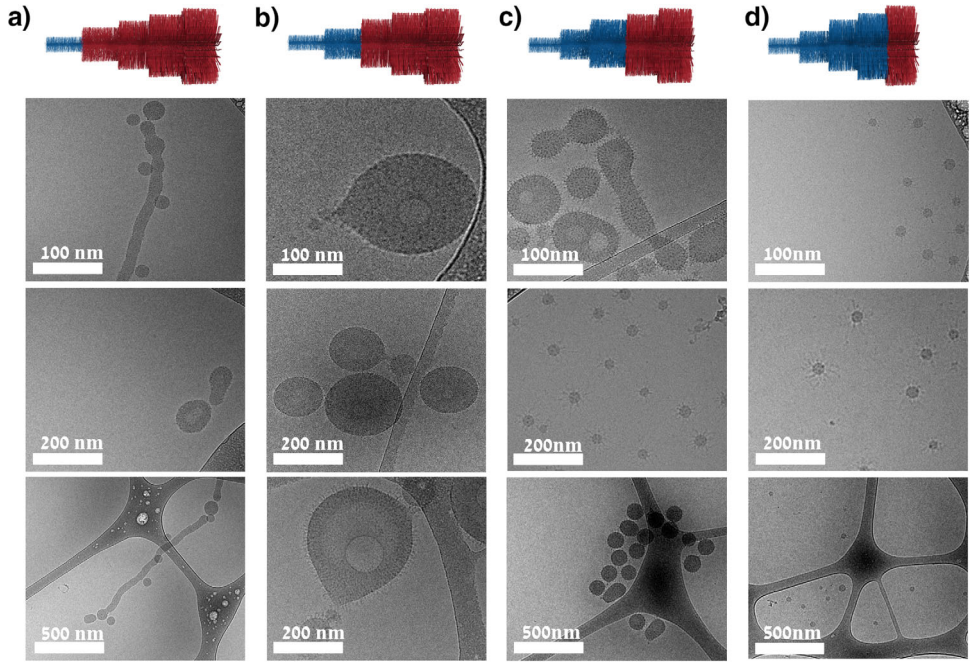

Figure 4. Cryo-TEM images of self-assembled aggregates of tapered bottlebrush BCPs **5**–**8** at three different levels of magnification. BCP **5** (column A) showed spherical structures with no clearly defined corona features, vesicles, and a few long cylindrical structures. BCP **6** (column B) showed approximately equal numbers of spherical micelles, larger spheres (semivesicles), and vesicles. BCP **7** (column C) showed a wide variety of nanostructures, including spherical micelles, cylindrical micelles, vesicles, semi-vesicles, and transitional structures between these nanostructures. BCP **8** (column D) showed only spherical micelles.

96 wt% hydrophobic, largely precipitated out during micelle formation. Analysis of the material that remained in solution showed a small number of nanostructures consisting primarily of two types of morphologies: spherical structures with no clearly defined protrusions (due to the very short hydrophilic components) and a smaller number of vesicles; a very small number of ellipsoids and cylinders were also observed. Images of BCP **6** (Figure 4b) revealed approximately equal numbers of spherical structures, larger spheres (semivesicles), and vesicles. BCP **7** (Figure 4c) also formed a wide variety of nanostructures, dominated by spherical micelles, semivesicles, and vesicles, some of which were budding, suggesting fusion or fission processes. BCP **7** also formed ellipsoids and cylindrical micelles. BCP **8** (Figure 4d) self-assembled into only spherical hairy micelles that were fairly uniform with a small fraction of larger spheres.

Heating and slow cooling BCPs **6** and **7**, with subsequent cryo-TEM imaging, revealed sheets and other very large, poorly defined aggregates (Figure S37). These results suggest that kinetically trapped nanostructures are present in these self-assembled BCP solutions.

*Cylindrical BCPs **9**–**12***

Images of the self-assembled cylindrical bottlebrush BCPs (BCPs **9**–**12)** are shown in Figure 5. BCP **9** (Figure 5a) formed mostly larger spheres, ellipsoids that appeared to be fusing spherical micelles, along with a few vesicles and spherical micelles. BCP **10** (Figure 5b) showed all classes of nanostructures described here, primarily larger spheres, ellipsoids, and cylinders, along with a small number of spherical micelles and vesicles. BCP **11** (Figure 5c) showed all morphologies aside from spherical micelles, primarily including vesicles, but also larger spheres (semivesicles), ellipsoids, and cylinders, as well as some large compound vesicles. BCP **12** (Figure 5d) largely precipitated out during the self-assembly step due to its high hydrophobic content. Cryo-TEM images of the remaining soluble portion of BCP **12** showed only vesicles and large compound vesicles.

Because BCP **10** exhibited many different types of aggregates, we chose to explore these morphologies more thoroughly in 3-dimensions using cryo-electron tomography. This method allows images to be collected in a tilt series, which can then be reconstructed into 3D tomograms. Figure 6 shows four pairs of images from the tomograms of BCP **10** with each including a whole particle thickness image (top row) and a slab from the *xy* plane in the middle of the tomogram (bottom row). These experiments showed the various morphologies with greater detail than the cryo-TEM images. For example, what initially appeared to be similar spherical structures of different sizes (Figure 6a and e) are actually two different morphologies (Figure 6b and f), several with filled cores (micelles) and several others with hollow cores (semi-vesicles). Vesicles with clear bilayers are observed in Figure 6c and g. Finally, ellipsoidal and extended cylindrical aggregates were observed in Figure 6d and h. A movie of the tomogram is available as supplementary information.

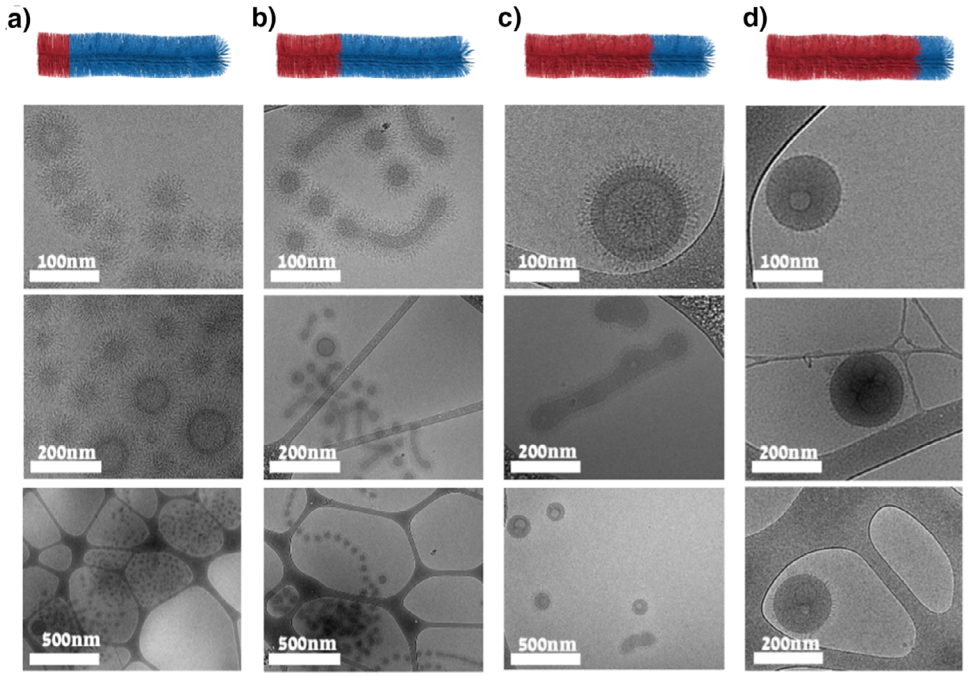

Figure 5. Cryo-TEM images of self-assembled aggregates of tapered bottlebrush BCPs **9**–**12** at three different levels of magnification. BCP **9** (column a) showed mostly larger spheres and a few vesicles. BCP **10** (column b) showed many types of aggregates and transitional structures. BCP **11** (column c) also showed a wide variety of nanostructures and transitional structures. BCP **12** (column d) showed only vesicles and large compound vesicles.

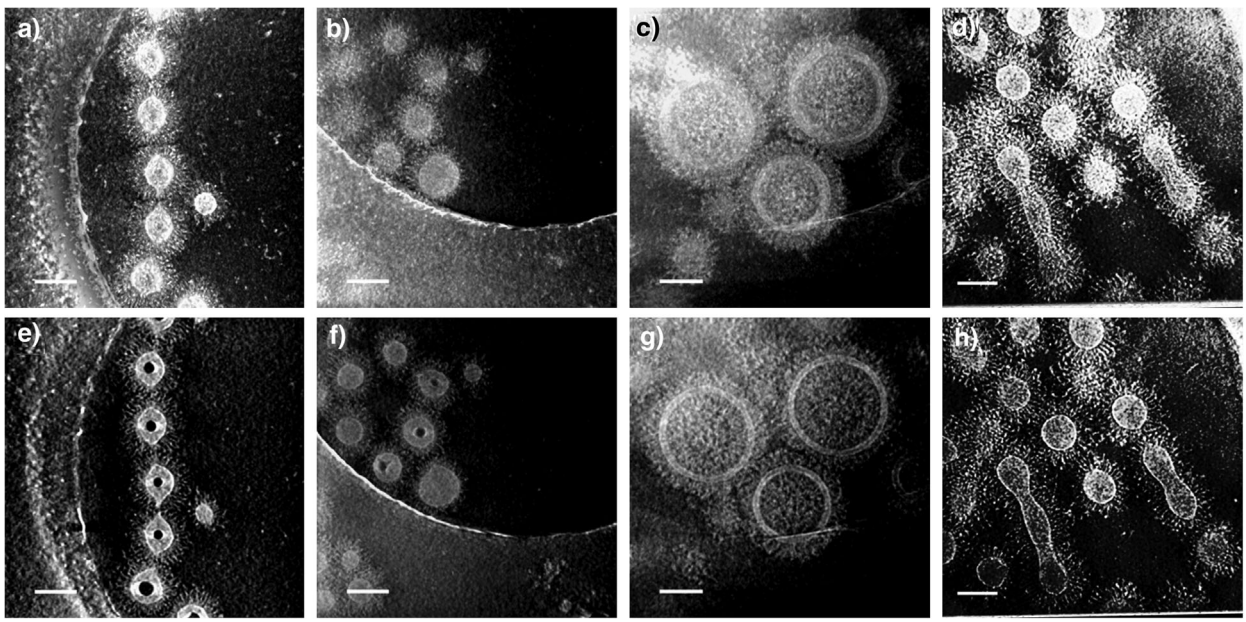

Figure 6. Cryo-electron tomography images of BCP **10**, reconstructed from an aligned tilt series. The top row (panels A–D) shows whole particle thickness images, and the bottom row (panels E–H) shows slabs from the *xy* plane in the middle of the tomogram. Multiple self-assembly pathways appear to be active in this BCP. Scale bar = 100 nm.

DLS, SANS, and Encapsulation Studies

In addition to cryo-TEM analysis, we also used dynamic light scattering (DLS) to characterize each of the bottlebrush BCP solutions to ascertain the hydrodynamic diameter and distribution profile of the tapered bottlebrush BCP nanostructures (Figure 7a–c). DLS results are presented as the number-weighted average diameter, and each sample showed a predominant size distribution with a polydispersity index (PDI) < 0.20, suggesting a relatively narrow size distribution and good uniformity among the assemblies. Notably, the intensity-weighted average diameter (Figure S35) was larger

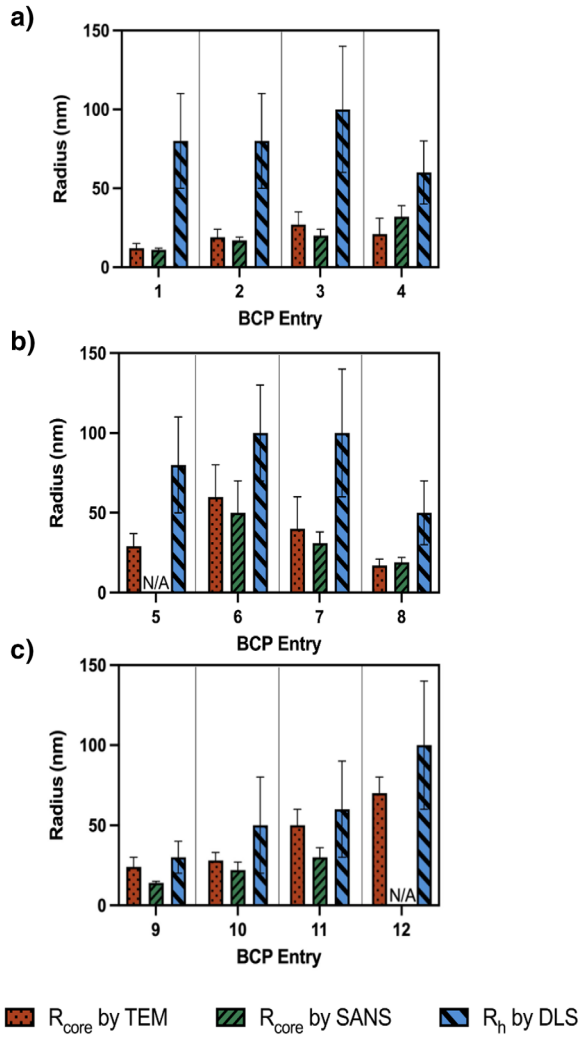

Figure 7. Core values based on cryo-TEM, SANS, and DLS for BCP assemblies **1**–**4** (panel a), **5**–**8** (panel b), and **9**–**12** (panel c). R_{core} values from cryo-TEM were estimated using visual analysis with ImageJ analyzing only the structures that were counted as micelles and larger spheres. R_{core} values from SANS were estimated using a combination of spheroid and unified fit models. Entries marked N/A did not show sufficient scattering signal to be fitted to the model. Hydrodynamic radius (R_h) values from DLS were estimated using the CONTIN fitting routine; number-average values are shown.

than the number-weighted average diameter, suggesting the presence of larger particles in the solutions, as was revealed by cryo-TEM for most samples.

We also studied each self-assembled bottlebrush BCP using small-angle neutron scattering (SANS). In these experiments, self-assembly was conducted using the same procedure as above but with D_2O instead of water. SANS profiles from these measurements (Figure S38) all showed continually increasing scattering intensity at low-q values, indicating the presence of elongated nanostructures and/or aggregates, likely induced by phosphate buffer (chosen due to its biological relevance), as noted previously by Pochan.[66] The mid-q to high-q regions showed scattering features of single scattering particles.

Fitting these SANS profiles to a single form factor was not possible. Therefore, we employed a combination of a power-law (P) model to account for contributions of the elongated and aggregated structures observed in the low-q region and a spheroid model to account for the scattering contribution from the hydrophobic cores of the bottlebrush BCP assemblies. Due to the high solvation of the hydrophilic PAA shell, there was not enough contrast to detect the shell, so only the hydrophobic core was observed in the measurements. These fittings allowed us to determine an average core radius (R_{core}) value for each self-assembled BCP nanostructure (Figure 7), except for bottlebrush BCPs **5** and **12**, which scattered weakly because a substantial amount of material precipitated out during the self-assembly step in these highly hydrophobic samples. We did not attempt to interpret the power laws observed at low-q because they likely result from contributions across multiple length scales, which is consistent with many of the cryo-TEM images. All fitting parameters are summarized in Table S9.

Comparing micelle R_{core} values between cryo-TEM measurements and SANS fittings showed that the sizes of the hydrophobic cores estimated by SANS largely agreed with the average sizes observed by cryo-TEM (Table 1). The trends in R_{core} size also generally matched expectations based on the size of the hydrophobic component, where greater hydrophobic content showed larger R_{core} values among each of the three sets (BCPs **1**–**4**, **5**–**8**, and **9**–**12**). There was one exception to this trend, which was the R_{core} values measured by cryo-TEM for BCPs **3** and **4**; this can likely be attributed to the tendency for micelles in BCP **4** to fuse to form elongated (cylindrical) structures, while micelles formed from BCP **3** instead appeared to grow into larger spheres. The radii obtained by DLS were naturally bigger than the radii obtained by SANS and TEM since DLS measures hydrodynamic radii based on the Stokes–Einstein equation, which includes the shell and the solvation layer as well as the particle's mobility in solution and not just the core structure.

It is clear from the results presented thus far that both the packing parameter and hydrophobic content guidelines failed to predict the dominant nanostructure in each of the self-assembled BCP solutions, although the wt% hydrophobic guidelines provided a slightly better prediction. These insights are highlighted by comparing the three bottlebrush BCPs with ~50 wt% hydrophobic content (BCPs **3**, **8,** and **10**). Traditional guidelines suggest that 50 wt% hydrophobic polymer amphiphiles are on the border between spherical micelles and cylindrical micelles. However, they all showed different morphological distributions (Figure 2). As discussed in detail above, BCP **3** (hydrophobic tip, 54 wt% hydrophobic) formed mostly spherical micelles with some ellipsoids and vesicles, while BCP **8** (hydrophilic tip, 53 wt% hydrophobic) formed almost exclusively spherical micelles and BCP **10** (cylindrical, 42 wt% hydrophobic) formed predominantly large spheres, cylinders, and ellipsoids.

We tested the encapsulation potential for this series of ~50 wt% hydrophobic nanostructures using the fluorescence of Nile red as a measure of how much of a model hydrophobic drug each type of nanostructure could encapsulate. There was no correlation between encapsulation ability and

nanostructure type, wt% hydrophobic, or spherical core radius, with BCP **8** encapsulating the least and BCP **3** approximately 3-fold more and BCP **10** in between these two extremes (Figure S39A). We performed a similar analysis and series of encapsulation studies on the three samples with ~70 wt% hydrophobic content (BCPs **4**, **7**, and **11**), all of which showed multiple types of nanostructures, and we also found no correlations (Figure S39B).

Simulations of Bottlebrush BCP Self-Assembly

As detailed above, no methods for rationalizing linear BCP self-assembly fully explained the wide variety of nanostructures, including transitional structures, observed in many of these bottlebrush BCP samples. There are two primary causes for this type of behavior in BCP self-assembly. First, in many linear BCPs, kinetic trapping is possible and even likely in many cases.[5,67–69] In the case of bottlebrush BCPs, multiple groups have recently used computational methods suggesting that non-equilibrium aggregates are quite common.[27,70] Second, the energy landscape for self-assembled nanostructures prepared from bottlebrush BCPs may be flatter and more easily manipulated than that for linear BCPs.[71] To shed further light on the self-assembly of these bottlebrush BCPs, we turned to coarse-grained (CG) molecular dynamics (MD) simulations.

We conducted implicit solvent CG MD simulations on the three BCPs with ~50 wt% hydrophobic content (BCPs **3**, **8**, and **10**). The hydrophobic interactions among the PS blocks were modeled using an attractive shifted-truncated Lennard–Jones potential, while the hydrophilic blocks were represented by repulsive Weeks–Chandler–Andersen beads. At pH 7, the hydrophilic blocks were deprotonated and carried a negative charge, with explicit counterions introduced to neutralize this charge. The structural properties of the individual bottlebrush macromolecules were characterized through the analysis of the average gyration tensor. The final trajectory of each single bottlebrush macromolecule simulation was used to define the initial state in each self-assembly simulation, packing the hydrophobic blocks of a fixed number of bottlebrush macromolecules into a defined volume, followed by equilibration to allow the system to relax and achieve a minimum energy configuration. This strategy expedites micelle formation, but we recognize that it limits the micelle fusion and possibly fission processes that occur in experiments. However, we envisioned that this method would allow us to estimate the critical aggregation number of bottlebrush macromolecules in a micelle for each of these BCP systems. The simulations were in a canonical ensemble, ensuring constant temperature through a Langevin thermostat, with time integration handled using the velocity-Verlet algorithm. All simulations were performed using LAMMPS. The simulation results are presented in Figure 8 in which hydrophilic side chains are omitted for clarity in images from the simulation trajectories in order to view the number of aggregates and shape of the cores.

For BCP **3**, structures resembling hairy micelles formed at five bottlebrush macromolecules (Figure 8a). As the number of bottlebrush macromolecules in the simulations increased, individual aggregates (spherical micelles) continued to grow up to 30 bottlebrush macromolecules, with some forming ellipsoidal structures. Above 30 bottlebrush macromolecules, simulations showed multiple smaller aggregates. Graphing normalized energy versus the number of bottlebrush macromolecules showed an initial drop from 5 to 10, then a plateau region, followed by another drop to lower energy around 30 as multiple aggregates formed. The results are consistent with the large size distribution of spherical and ellipsoidal aggregates that dominate the cryo-TEM images for BCP **3**.

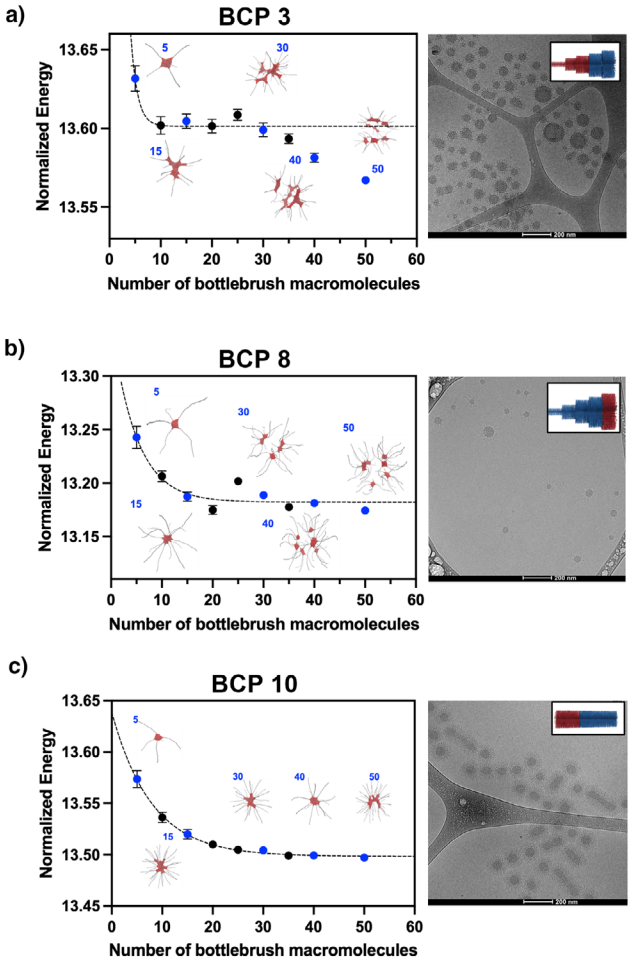

Figure 8. BCP self-assembly simulations, representative cryo-TEM images, and schematic structural representations of BCPs **3** a), **8** b), and **10** c). The "normalized energy" is the total energy, which is the sum of the potential and kinetic energy of the simulation, divided by the total number of beads in the simulation box, in units of thermal energy, k_BT. The trendline is an exponential decay function, $E(n) = Ae^{(-n/n_c)} + B$, where E is the normalized energy as a function of the number of bottlebrush macromolecules in the simulation box (n), A and B are fitting constants, and n_c is a characteristic number. In the images of the simulation trajectories within the graphs, the red components represent the PS side chains, and the grey lines represent the polynorbornene backbone. The PAA components are omitted for clarity because they are largely invisible in the cryo-TEM images. See Figures S41–S43 for more detailed images. Descriptions of shapes (e.g., ellipsoids, cylinders) follow the same aspect ratio values as were used in the cryo-TEM studies.

A few vesicles were also present in the cryo-TEM images, but the simulations were limited in size and in the number of bottlebrush molecules, and therefore, could not capture these vesicles due to the long timescales and large number of bottlebrush macromolecules required for vesicle formation.

Similar simulations of BCP **8** (Figure 8b) showed the formation of individual small aggregates of up to 50 bottlebrush macromolecules, with most favoring spherical shapes. These simulation results are consistent with the cryo-TEM images, which showed almost exclusively spherical micelles along with a few ellipsoids. The graph of energy versus bottlebrush macromolecules plateaued around 15 bottlebrush macromolecules and stayed flat. These results suggest that spherical aggregates are the equilibrium morphology for this bottlebrush BCP.

Finally, simulations on BCP **10** (Figure 8c) showed that this cylindrical bottlebrush BCP favored the formation of elongated structures (ellipsoids and short cylinders), forming a single cylindrical structure at 50 bottlebrush macromolecules. These simulations were also consistent with the cryo-TEM images, which showed primarily larger spheres, ellipsoids, and cylinders. There was a gradual decline in the plot of energy versus the number of bottlebrush macromolecules.

Self-Assembly Pathways

In linear amphiphilic BCPs, two pathways toward more complex morphologies are typically considered.[72–74] Both begin with self-assembly into spherical micelles, although recent experimental and theoretical work from Sommerdijk, Patterson, and coworkers indicates that a liquid–liquid phase separation step precedes micelle formation, at least in some amphiphilic linear BCPs.[75] After the formation of metastable micelles, one pathway that leads to more complex self-assembled morphologies is fusion of spherical micelles into ellipsoids, which further fuse to form cylindrical nanostructures. In the other proposed pathway toward more complex aggregates, spherical micelles transform into semivesicles, which can take on either spherical or ellipsoidal shapes. Liquid–liquid separation may again play a role here, in particular in defining the size of the semivesicles and eventual vesicles, as suggested by He and Schmid in their work on linear BCPs.[76] Semivesicles mature through solvent diffusion, growing larger to become vesicles with an identifiable solvent-filled core. In some cases, the vesicles then fuse to become large compound vesicles. The pathways taken and even the sizes of the ultimate nanostructures are likely controlled through interaction parameters between the two blocks and between each block and solvent, as well as polymer parameters (e.g., molecular weight and weight fraction of the two blocks).[75]

Our collective results suggest that the evolution of self-assembled morphologies in these samples follows similar pathways (Figure 9). As with most amphiphilic BCPs of any topology, spherical micelles appear to be the first morphology to form for most of the 12 bottlebrush BCPs (all samples except BCP **11** showed at least a few spherical micelles). Some samples never progressed beyond spherical micelles. BCPs **1** and **2** are good examples, where spherical micelles dominate in BCP **1**, and a mixture of spherical micelles and larger spheres appear in BCP **2** (these larger spheres all appear to have micellar structures). These structures follow traditional guidelines for rationalizing self-assembly pathways as the bottlebrush BCPs have relatively little hydrophobic content. In the hydrophilic tip series, BCP **8** also formed only spherical micelles, likely because of the long hydrophilic component stabilizing the bulkier but much shorter hydrophobic domain.

The pathway leading toward cylindrical aggregates (Figure 9, top pathway) is best exhibited by BCP **10**, which clearly shows extended aggregates in both the cryo-TEM images and the simulations. BCP **4** also exhibited several cylindrical nanostructures, and cryo-TEM images revealed fusing micelles and elliptical aggregates along this pathway. The pathway toward vesicles and large compound vesicles (Figure 8, bottom pathway) involves intermediate semivesicles. The evolution of nanostructures along this pathway is best exhibited by BCPs **6** and **9**, where semivesicles coexist with vesicles in the TEM images. The cryo-electron tomography images of BCP **10** (Figure 6) also highlight the semivesicle structures. To our knowledge, these images represent the first experimental evidence of this pathway to vesicle formation in bottlebrush BCPs. Taken together, the cryo-TEM images of these 12 bottlebrush BCPs suggest that, in many cases, micelles mature into more complex nanostructures along one or sometimes both of these pathways, suggesting that bottlebrush BCPs may be able to explore the self-assembly energy landscape more thoroughly than linear BCPs. More studies on a wider variety of cylindrical and tapered bottlebrush BCPs are required to fully describe the self-assembly landscape.

Conclusions

In summary, we synthesized a series of 12 tapered and cylindrical bottlebrush BCPs. The synthesis involved the preparation and careful purification of five PS and five PtBA macromonomers, followed by SAM-ROMP to prepare bottlebrush BCPs, and finally, a hydrolysis step to form the target amphiphilic bottlebrush BCPs. The polymers were designed as three groups of four—one group with a hydrophobic tip (**1**–**4**), one group with a hydrophilic tip (**5**–**8**), and one group of cylindrical bottlebrush polymers (**9**–**12**). Within each group, the hydrophobic content varied. Self-assembly was induced in each bottlebrush BCP using the solvent-switch method. Each solution was then characterized using cryo-TEM, DLS, and SANS, and these techniques combined with CG MD simulations provided a comprehensive view of the various self-assembled nanostructures formed by these large polymeric amphiphiles. Nearly all cryo-TEM images revealed surface protrusions, a result of the bottlebrush structure. Heating and cooling studies on selected self-assembled BCPs indicated that kinetic trapping occurred for some but not all BCP structures, and other self-assembly methods that promote micelle–unimer exchange might reveal different distributions of nanostructures. Despite some kinetically trapped structures, we were able to draw several conclusions.

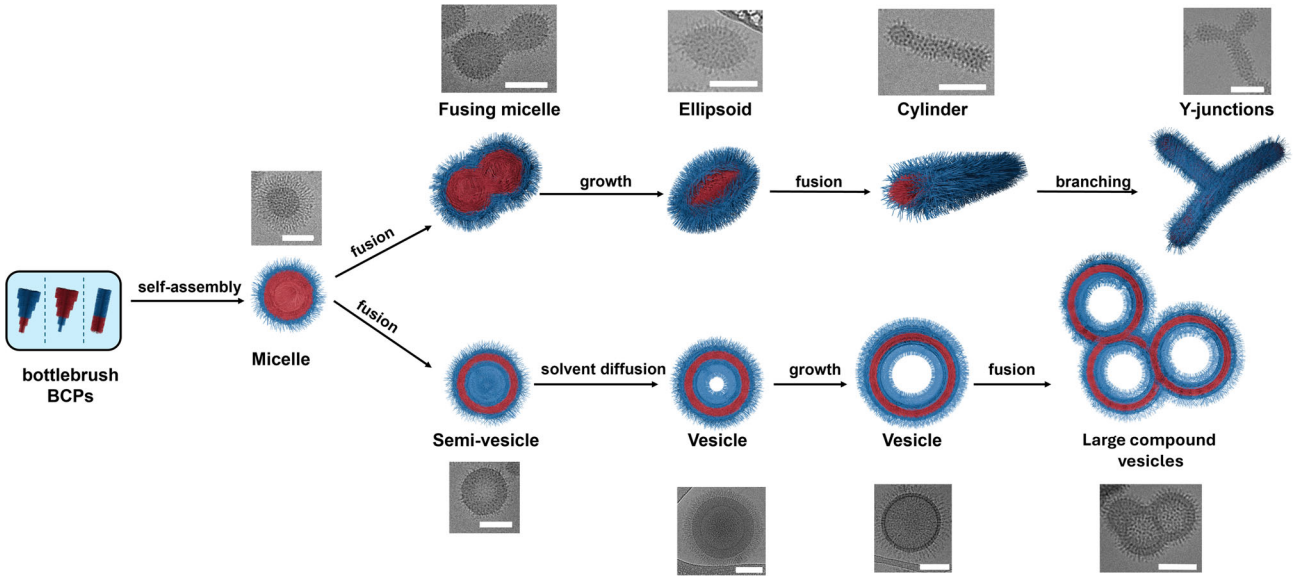

Figure 9. Schematic illustrations and representative cryo-TEM images of self-assembly pathways of bottlebrush BCPs (scale bar = 100 nm).

Overall, we found that BCP micelles frequently evolve into more complex nanostructures via two pathways. One involves micelle fusion to form cylindrical aggregates, which sometimes form Y-junctions. The other involves micelle maturation into semivesicles, which eventually form vesicles and sometimes large compound vesicles. These studies provide the first experimental evidence supporting the proposed pathway for vesicle formation via semivesicles in bottlebrush BCPs. Collectively, these results imply that bottlebrush BCPs may explore the self-assembly energy landscape more comprehensively than their linear counterparts. Due to the many tunable structural parameters in bottlebrush BCPs, these 12 bottlebrush BCPs represent only a tiny fraction of the possible chemical structures accessible using these synthetic techniques. We anticipate that further experimental and computational studies on amphiphilic bottlebrush BCPs will continue to reveal interesting self-assembled nanostructures and shed further light on the solution self-assembly pathways available to these unusual polymeric amphiphiles.

Supporting Information

The authors have cited additional references within the Supporting Information.[77]

Acknowledgements

This work was supported by a joint grant from the US National Science Foundation (DMR-2104602) and the US-Israel Binational Science Foundation (NSF-BSF 2020715). The authors thank Prof Rana Ashkar for helpful discussions and Daniela Samaniego Gonzalez for assistance with running SANS experiments, as well as the team at the BIO-SANS beamline. The authors thank the Virginia Tech Mass Spectrometry Research Incubator for high-resolution mass spectrometry analysis and the Virginia Tech Department of Chemistry Analytical Facilities for NMR usage. A portion of this research used resources at the High Flux Isotope Reactor and the Spallation Neutron Source, a DOE Office of Science User Facility operated by the Oak Ridge National Laboratory. The beam time was allocated to BioSANS on proposal number IPTS-31356.1 and EQ-SANS on 25165.1. Modeling and simulations were conducted as part of a user project at the Center for Nanophase Materials Sciences (CNMS), which is a US Department of Energy, Office of Science User Facility at Oak Ridge National Laboratory. This research used resources of the Oak Ridge Leadership Computing Facility at the Oak Ridge National Laboratory, which is supported by the Office of Science of the U.S. Department of Energy under Contract No. DE-AC05-00OR22725. The authors are grateful for the generous support from the Guzik Foundation to BGU's cryo-electron microscopy unit.

Conflict of Interests

The authors declare no conflict of interest.

Data Availability Statement

The data that support the findings of this study are openly available in [figshare.com]: at [https://doi.org/10.6084/m9.figshare.28156775], reference number [28156775].

Keywords: Atom-transfer radical polymerization · Cryo-electron tomography · Grubbs third generation catalyst · Semi-vesicles · Size exclusion chromatography with multi-angle light scattering

[1] M. Karayianni, S. Pispas, *J. Polym. Sci.* **2021**, *59*, 1874–1898.

[2] H. Feng, X. Lu, W. Wang, N.-G. Kang, J. W. Mays, *Polymers* **2017**, *9*, 494.
[3] C. M. Bates, F. S. Bates, *Macromolecules* **2017**, *50*, 3–22.
[4] J. N. Israelachvili, D. J. Mitchell, B. W. Ninham, *J. Chem. Soc., Faraday Trans. 2* **1976**, *72*, 1525.
[5] Y. Mai, A. Eisenberg, *Chem. Soc. Rev.* **2012**, *41*, 5969.
[6] S. Venkataraman, J. L. Hedrick, Z. Y. Ong, C. Yang, P. L. R. Ee, P. T. Hammond, Y. Y. Yang, *Adv. Drug Delivery Rev* **2011**, *63*, 1228–1246.
[7] P. A. Mistark, S. Park, S. E. Yalcin, D. H. Lee, O. Yavuzcetin, M. T. Tuominen, T. P. Russell, M. Achermann, *ACS Nano* **2009**, *3*, 3987–3992.
[8] N. Hadjichristidis, H. Iatrou, M. Pitsikalis, S. Pispas, A. Avgeropoulos, *Prog. Polym. Sci.* **2005**, *30*, 725–782.
[9] R. J. Williams, A. P. Dove, R. K. O'Reilly, *Polym. Chem.* **2015**, *6*, 2998–3008.
[10] J. C. Foster, S. Varlas, B. Couturaud, Z. Coe, R. K. O'Reilly, *J. Am. Chem. Soc.* **2019**, *141*, 2742–2753.
[11] S. Dutta, M. A. Wade, D. J. Walsh, D. Guironnet, S. A. Rogers, C. E. Sing, *Soft Matter* **2019**, *15*, 2928–2941.
[12] I. O. Lebedeva, E. B. Zhulina, O. V. Borisov, *Polymers* **2021**, *13*, 1351.
[13] S. E. Blosch, S. J. Scannelli, M. Alaboalirat, J. B. Matson, *Macromolecules* **2022**, *55*, 4200–4227.
[14] R. Liu, Z. Sun, H. Huang, J. A. Johnson, A. Alexander-Katz, C. A. Ross, *Nano Lett.* **2023**, *23*, 177–182.
[15] H. Zeng, X. Liang, D. A. Roberts, E. R. Gillies, M. Müllner, *Angew. Chem. Int. Ed.* **2024**, *63*, e202318881.
[16] L. Liberman, M. L. Coughlin, S. Weigand, F. S. Bates, T. P. Lodge, *Macromolecules* **2022**, *55*, 2821–2831.
[17] W. Liu, Y. Liu, G. Zeng, R. Liu, Y. Huang, *Polymer* **2012**, *53*, 1005–1014.
[18] S. J. Dalsin, M. A. Hillmyer, F. S. Bates, *Macromolecules* **2015**, *48*, 4680–4691.
[19] H. Liang, G. S. Grest, A. V. Dobrynin, *ACS Macro Lett.* **2019**, *8*, 1328–1333.
[20] M. Alaboalirat, L. Qi, K. J. Arrington, S. Qian, J. K. Keum, H. Mei, K. C. Littrell, B. G. Sumpter, J.-M. Y. Carrillo, R. Verduzco, J. B. Matson, *Macromolecules* **2019**, *52*, 465–476.
[21] Y. Wang, F. Shao, E. R. Sauvé, C. M. Tonge, Z. M. Hudson, *Soft Matter* **2019**, *15*, 5421–5430.
[22] J. F. Hassler, N. J. Van Zee, A. A. Crabtree, F. S. Bates, B. J. Hackel, T. P. Lodge, *ACS Macro Lett.* **2022**, *11*, 460–467.
[23] E. Ahmed, C. T. Womble, M. Weck, *Macromolecules* **2020**, *53*, 9018–9025.
[24] F. Shao, Y. Wang, C. M. Tonge, E. R. Sauvé, Z. M. Hudson, *Polym. Chem.* **2020**, *11*, 1062–1071.
[25] M. G. Wessels, A. Jayaraman, *Soft Matter* **2019**, *15*, 3987–3998.
[26] T. Pan, B. B. Patel, D. J. Walsh, S. Dutta, D. Guironnet, Y. Diao, C. E. Sing, *Macromolecules* **2021**, *54*, 3620–3633.
[27] B. Gumus, M. Herrera-Alonso, A. Ramírez-Hernández, *Soft Matter* **2020**, *16*, 4969–4979.
[28] S. Kwon, J. Nam, J. W. Chung, M. Seo, W. B. Lee, Y. Kim, *Macromolecules* **2024**, *57*, 7664–7674.
[29] L. Liberman, M. L. Coughlin, S. Weigand, J. Edmund, F. S. Bates, T. P. Lodge, *Macromolecules* **2022**, *55*, 4947–4955.
[30] R. Fenyves, M. Schmutz, I. J. Horner, F. V. Bright, J. Rzayev, *J. Am. Chem. Soc.* **2014**, *136*, 7762–7770.
[31] H. Unsal, S. Onbulak, F. Calik, M. Er-Rafik, M. Schmutz, A. Sanyal, J. Rzayev, *Macromolecules* **2017**, *50*, 1342–1352.
[32] K. R. Gadelrab, A. Alexander-Katz, *J. Phys. Chem. B* **2020**, *124*, 11519–11529.
[33] H. Ma, K. T. Kim, *Macromolecules* **2020**, *53*, 711–718.
[34] G. P. Sorenson, K. L. Coppage, M. K. Mahanthappa, *J. Am. Chem. Soc.* **2011**, *133*, 14928–14931.
[35] S. D. Hudson, H. T. Jung, V. Percec, W. D. Cho, G. Johansson, G. Ungar, V. S. K. Balagurusamy, *Science* **1997**, *278*, 449–452.
[36] V. S. K. Balagurusamy, G. Ungar, V. Percec, G. Johansson, *J. Am. Chem. Soc.* **1997**, *119*, 1539–1555.
[37] M. N. Holerca, D. Sahoo, B. E. Partridge, M. Peterca, X. Zeng, G. Ungar, V. Percec, *J. Am. Chem. Soc.* **2018**, *140*, 16941–16947.
[38] K. Yue, C. Liu, M. Huang, J. Huang, Z. Zhou, K. Wu, H. Liu, Z. Lin, A.-C. Shi, W.-B. Zhang, S. Z. D. Cheng, *Macromolecules* **2017**, *50*, 303–314.
[39] X. Yu, S. Zhong, X. Li, Y. Tu, S. Yang, R. M. Van Horn, C. Ni, D. J. Pochan, R. P. Quirk, C. Wesdemiotis, W.-B. Zhang, S. Z. D. Cheng, *J. Am. Chem. Soc.* **2010**, *132*, 16741–16744.
[40] W. Zhang, X. Lu, J. Mao, C.-H. Hsu, G. Mu, M. Huang, Q. Guo, H. Liu, C. Wesdemiotis, T. Li, W.-B. Zhang, Y. Li, S. Z. D. Cheng, *Angew. Chem. Int. Ed.* **2017**, *56*, 15014–15019.
[41] S.-M. Yang, S.-H. Kim, J.-M. Lim, G.-R. Yi, *J. Mater. Chem.* **2008**, *18*, 2177.
[42] F. Hagemans, E. B. van der Wee, A. van Blaaderen, A. Imhof, *Langmuir* **2016**, *32*, 3970–3976.
[43] F. Yuan, X. Zhang, M. Yang, W. Wang, B. Minch, G. Lieser, G. Wegner, *Soft Matter* **2007**, *3*, 1372.
[44] S. C. Glotzer, M. J. Solomon, *Nat. Mater.* **2007**, *6*, 557–562.
[45] T. Chen, Z. Zhang, S. C. Glotzer, *Langmuir* **2007**, *23*, 6598–6605.
[46] S. Sacanna, D. J. Pine, G.-R. Yi, *Soft Matter* **2013**, *9*, 8096.
[47] S. Y. Joshi, S. Singh, S. A. Deshmukh, *npj Comput. Mater.* **2022**, *8*, 45.
[48] S. C. Radzinski, J. C. Foster, S. J. Scannelli, J. R. Weaver, K. J. Arrington, J. B. Matson, *ACS Macro Lett.* **2017**, *6*, 1175–1179.
[49] M. Alaboalirat, S. J. Scannelli, H. Rahmaninejad, J.-M. Carrillo, C. Do, J. B. Matson, R. Ashkar, *Macromolecules* **2023**, *56*, 9264–9276.
[50] D. J. Walsh, S. Dutta, C. E. Sing, D. Guironnet, *Macromolecules* **2019**, *52*, 4847–4857.
[51] D. J. Walsh, D. Guironnet, *Proc. Natl. Acad. Sci. USA* **2019**, *116*, 1538–1542.
[52] M. Alaboalirat, C. Vu, J. B. Matson, *Polym. Chem.* **2022**, *13*, 5841–5851.
[53] S. J. Scannelli, A. Paripati, J. R. Weaver, C. Vu, M. Alaboalirat, D. Troya, J. B. Matson, *Macromolecules* **2023**, *56*, 3848–3856.
[54] S. J. Scannelli, M. Alaboalirat, D. Troya, J. B. Matson, *Macromolecules* **2023**, *56*, 3838–3847.
[55] N. D. Ogbonna, M. Dearman, C.-T. Cho, B. Bharti, A. J. Peters, J. Lawrence, *JACS Au* **2022**, *2*, 898–905.
[56] S. E. Blosch, M. Alaboalirat, C. B. Eades, S. J. Scannelli, J. B. Matson, *Macromolecules* **2022**, *55*, 3522–3532.
[57] S. L. Pesek, X. Li, B. Hammouda, K. Hong, R. Verduzco, *Macromolecules* **2013**, *46*, 6998–7005.
[58] A. D. Filippov, I. A. van Hees, R. Fokkink, I. K. Voets, M. Kamperman, *Macromolecules* **2018**, *51*, 8316–8323.
[59] M. Fauquignon, L. Porcar, A. Brûlet, J.-F. Le Meins, O. Sandre, J.-P. Chapel, M. Schmutz, C. Schatz, *ACS Macro Lett.* **2023**, *12*, 1272–1279.
[60] N. P. Iakimov, M. A. Zotkin, E. A. Dets, S. S. Abramchuk, A. M. Arutyunian, I. D. Grozdova, N. S. Melik-Nubarov, *Colloid Polym. Sci.* **2021**, *299*, 1543–1555.
[61] S. Förster, B. Berton, H. P. Hentze, E. Krämer, M. Antonietti, P. Lindner, *Macromolecules* **2001**, *34*, 4610–4623.
[62] U. Tritschler, S. Pearce, J. Gwyther, G. R. Whittell, I. Manners, *Macromolecules* **2017**, *50*, 3439–3463.
[63] D. E. Discher, F. Ahmed, *Annu. Rev. Biomed. Eng.* **2006**, *8*, 323–341.
[64] Z. Deng, S. Liu, *Polymer* **2020**, *207*, 122914.
[65] C. Contini, R. Pearson, L. Wang, L. Messager, J. Gaitzsch, L. Rizzello, L. Ruiz-Perez, G. Battaglia, *iScience* **2018**, *7*, 132–144.
[66] N. J. Sinha, R. Guo, R. Misra, J. Fagan, A. Faraone, C. J. Kloxin, J. G. Saven, G. V. Jensen, D. J. Pochan, *J. Colloid Interface Sci.* **2022**, *606*, 1974–1982.

[67] H. Cui, Z. Chen, S. Zhong, K. L. Wooley, D. J. Pochan, *Science* **2007**, *317*, 647–650.
[68] S. D. P. Fielden, *J. Am. Chem. Soc.* **2024**, *146*, 18781–18796.
[69] W.-D. He, X.-L. Sun, W.-M. Wan, C.-Y. Pan, *Macromolecules* **2011**, *44*, 3358–3365.
[70] E. Mohammadi, S. Y. Joshi, S. A. Deshmukh, *Comput. Mater. Sci.* **2021**, *199*, 110720.
[71] Z. Gan, D. Zhou, Z. Ma, M. Xu, Z. Xu, J. He, J. Zhou, X.-H. Dong, *J. Am. Chem. Soc.* **2023**, *145*, 487–497.
[72] S. Iqbal, M. Blenner, A. Alexander-Bryant, J. Larsen, *Biomacromolecules* **2020**, *21*, 1327–1350.
[73] J. F. Le Meins, O. Sandre, S. Lecommandoux, *Euro. Phys. J. E* **2011**, *34*, 14.
[74] D. J. Adams, S. Adams, D. Atkins, M. F. Butler, S. Furzeland, *J. Controlled Release* **2008**, *128*, 165–170.
[75] A. Ianiro, H. Wu, M. M. J. van Rijt, M. P. Vena, A. D. A. Keizer, A. C. C. Esteves, R. Tuinier, H. Friedrich, N. A. J. M. Sommerdijk, J. P. Patterson, *Nat. Chem.* **2019**, *11*, 320–328.
[76] X. He, F. Schmid, *Macromolecules* **2006**, *39*, 2654–2662.
[77] J. Liu, A. X. Gao, J. A. Johnson, *J. Vis. Exp.* **2013**, *80*, 1940–087X.

Manuscript received: January 09, 2025
Revised manuscript received: March 06, 2025
Accepted manuscript online: April 01, 2025
Version of record online: April 25, 2025